Influence of yield-surface shape in simulation of ballistic impact

Jens Kristian Holmen*, Odd Sture Hopperstad, Tore Børvik

Structural Impact Laboratory (SIMLab), Department of Structural Engineering, Norwegian University of Science and Technology (NTNU), NO-7491 Trondheim, Norway

Centre for Advanced Structural Analysis (CASA), NTNU, NO-7491, Trondheim, Norway

Abstract

A high-exponent yield criterion is applied in 3D nonlinear finite element simulations of ballistic impact. The computational models are based on a comprehensive experimental study including material tests of 12 mm thick high-strength Weldox 700 E steel plates and ballistic tests where the plates were struck by blunt-nosed and ogive-nosed projectiles with a diameter of 20 mm and a mass of approximately 200 g. We thoroughly describe the constitutive model and the numerical modeling procedure. The simulation results are discussed in light of the perforation mechanisms as well as the experimental results. Changing the shape of the yield surface in the deviatoric plane increases the residual velocity of the projectile and the effect was largest in simulations with the blunt-nosed projectile. Although the difference in residual velocity can be significant close to the ballistic limit velocity, the variation in predicted ballistic limit velocity itself was not more than 7 %. To put this into context, the effect of the yield-surface shape was compared to the effects of changing the parameters controlling friction, rate sensitivity, adiabatic heating, and temperature softening. These results suggest that a high-exponent yield criterion is not essential for ordinary steels and aluminum alloys where moderate yield-surface exponents are expected.

Keywords: Projectile penetration, Steel plates, Ballistic limit velocity, Finite element analysis, Hershey yield function, Johnson-Cook

1. Introduction

The von Mises yield criterion is by far the most wide-spread yield criterion in ballistic simulations and it is used, by default, but in general with success, for most types of metals and alloys. It assumes

*Corresponding author. Tel.: +47 930 45 837
Email address: jens.k.holmen@ntnu.no (Jens Kristian Holmen)

that yielding occurs when the second principal invariant of the deviatoric stress tensor, J_2, reaches a critical value. Hence the name J_2 flow theory which is frequently used for plasticity theories based on the von Mises yield criterion. Further assumptions include isotropy and pressure insensitivity of the material, meaning that the yield locus is a right cylinder aligned along the hydrostatic axis in stress space. This yield locus can be changed by making it dependent on the hydrostatic stress or by altering its shape in the deviatoric Π-plane. Dependency on the hydrostatic stress is important in frictional materials such as concrete, rock and soils, but also for foams and some polymers where the behavior in compression is different from the behavior in tension. This is most aptly introduced in models by changing the shape of the locus from a right cylinder into a cone [1]. Changing the shape in the Π-plane can be done by retaining isotropy [2, 3], or by introducing anisotropy [4, 5]. The latter can be vital in for instance rolled aluminum plates where the behavior in the rolling direction is different from the behaviors in the transverse and thickness directions of the plate.

There are many examples of impact-related studies that use J_2 plasticity and Johnson-Cook (JC) [6] type constitutive relations to simulate isotropic, and not so isotropic, materials [7–10]. Arias et al. [11] simulated the impact behavior of thin steel plates struck by projectiles with various nose shapes using the JC model. Iqbal et al. [12, 13] studied Weldox 460 E steel plates and AA1100-H12 aluminum alloy plates, and Manes et al. [14] looked at the perforation and penetration behavior of AA6061-T6 aluminum alloy. A slightly different area of application was explored by Aune et al. [15] who recently used J_2 plasticity to study blast effects on rather anisotropic aluminum sheets.

Given the dissemination of J_2 plasticity, there are surprisingly few studies where the effects of the shape of the yield surface have been examined in a systematic manner for ballistic impact problems. Models where the third deviatoric stress invariant J_3, or the Lode parameter L, is accounted for have been presented by for instance Bai and Wierzbicki [16] and Chocron et al. [17] where the latter model was applied in ballistic impact simulations. They also considered Lode dependent failure loci.

A proper description of material anisotropy is imperative when modeling, for example, composites, but for metals this is often disregarded. Grytten et al. [18] reported limited effects when they included an anisotropic yield function (YLD2004-18p [5]) in numerical simulations of low-velocity impact. Conversely, Seidt et al. [19] looked at the effect of using an anisotropic yield surface in blunt-nosed projectile impact of aluminum sheets and plates. They conclude that the shape of the yield surface affects the results of ballistic impact simulations when using a six-component anisotropic yield function [20], suggesting that the shape of the yield surface does, in fact, influence the ballistic behavior.

The response of plates struck by projectiles of different shapes, particularly blunt-nosed and ogive-nosed projectiles, is vastly different. Chiefly, we can say that blunt-nosed projectiles induce plugging failure in intermediate thick plates. Here, bands of intense shear, often helped by adiabatic heating, cut through the plate which promotes the formation of a plug with the same diameter as the circumference of the projectile. Such shear bands have been found to be thinner than 10 μm for Weldox 700 E steel plate [21] and they complicate the simulation procedure for perforation by projectiles with flat noses. In the case of ogive-nosed projectiles the main perforation mechanism is ductile hole growth where the pointed projectile tip pushes material perpendicularly to the flight direction meaning that plastic dissipation takes place in a much larger portion of the plate than for blunt-nosed projectiles.

In this work, we study systematically how the shape of the yield surface affects the results of ballistic impact simulations. Previously obtained experimental data is revisited and will provide context to the numerical simulations. The isotropic and pressure independent high-exponent yield function is then presented along with the constitutive relation and the failure criterion. Ballistic impact simulations with varying yield surfaces, initial velocities and projectile nose shapes are presented before the results are discussed in the closing section.

2. Material and experimental tests

2.1. Weldox 700 E steel plates

Comprehensive experimental works on Weldox 700 E steel plates by Dey et al. [21] serve as the backdrop for the study of the yield-surface shape in this paper. Weldox 700 E is a quenched and tempered martensitic steel with high strength and high ductility. To calibrate the constitutive relation, Dey et al. [21] conducted uniaxial and notched quasi-static tension tests, tension tests at elevated strain rates and tension tests at elevated temperatures. Figure 1 shows (a) the equivalent stress-strain curve, (b) the influence of stress triaxiality on the fracture strain, (c) the strain rate sensitivity, and (d) the temperature dependence of Weldox 700 E. The fracture strain is about 1.2 for smooth quasi-static tension tests and it decreases significantly with increased stress triaxiality ratio. The flow stress is sensitive to the strain rate and increasing the strain rate increases the stress (Figure 1c). For increasing temperature, the yield stress drops as seen in Figure 1d. Dey et al. [21] also reported that the fracture strain increased with temperature, but that the strain rate hardly affected the ductility of the material.

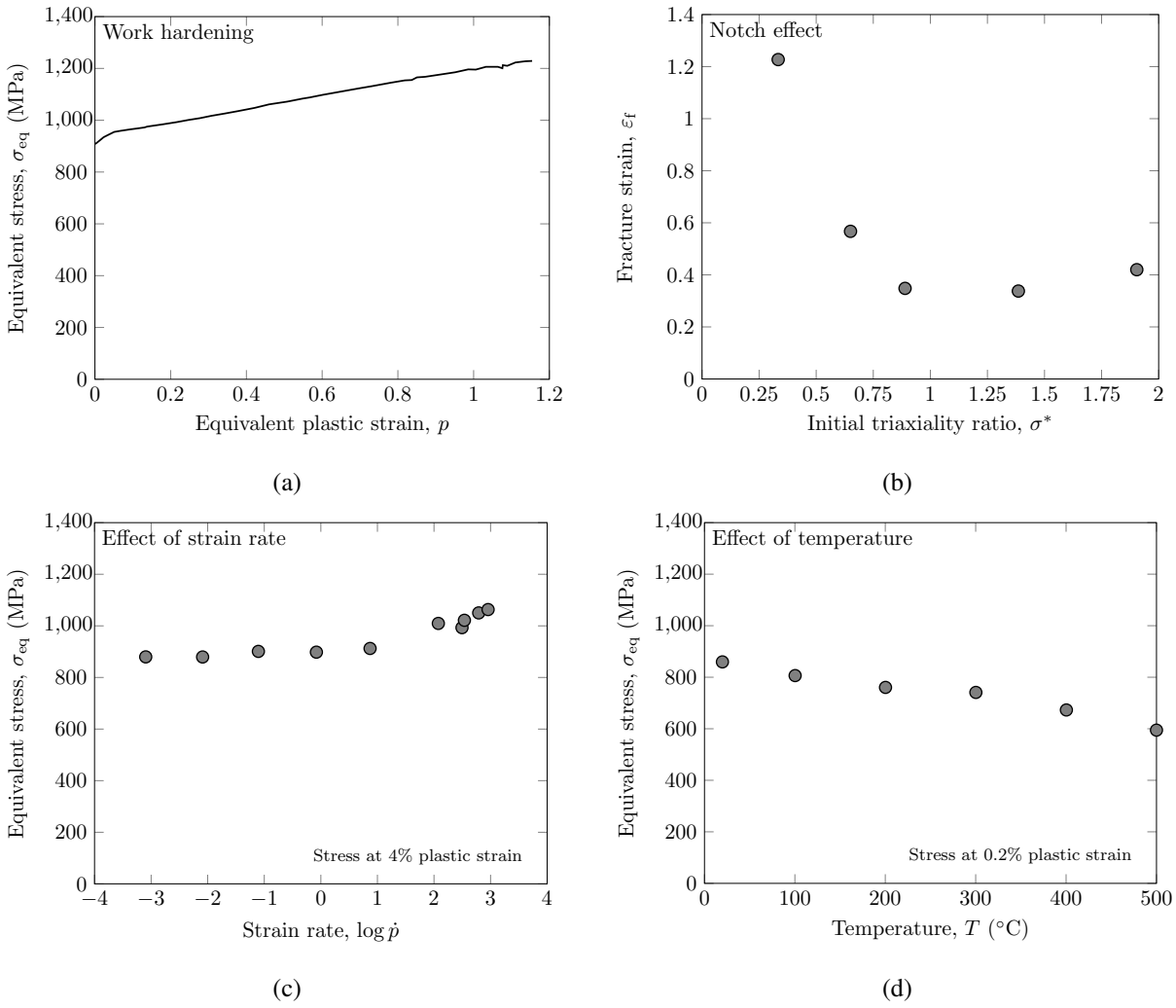

Figure 1: Experimental data from the material tests of Dey et al. [21]

2.2. Ballistic testing

Sabot-mounted blunt-nosed and ogive-nosed hardened steel projectiles were launched toward 12 mm thick Weldox 700 E steel plates at impact velocities between 150 m/s and 370 m/s. The tests were conducted in a compressed gas gun that has been used frequently to study the perforation behavior of various targets, see for example Refs. [7, 9, 10]. Various optical measurement systems obtained the velocity of the projectile before and after perforation [9]. The target plates had a free span of 500 mm and were clamped to the circular test fixture with 21 pre-stressed M16 bolts. Only one test was conducted per plate.

The cylindrical projectiles (Figure 2) have a nominal mass of 197 g and a nominal diameter of 20 mm. They are made of hardened Arne tool steel with a Rockwell C hardness of 51-53 corresponding to a yield

stress of about 1700 MPa. The blunt-nosed projectile is an 80 mm long, right cylinder while the total length of the ogive-nosed projectile is 95 mm of which 33 mm has a caliber radius head (CRH) of 3.

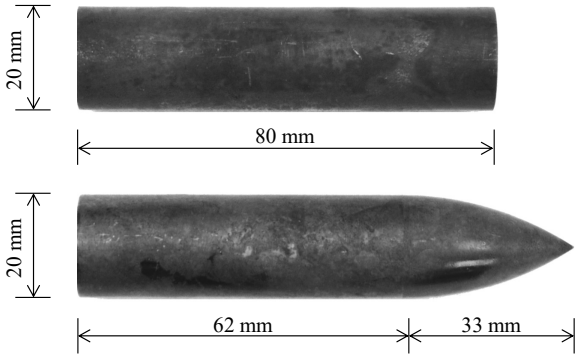

Figure 2: Dimensions of the blunt-nosed (top) and ogive-nosed (bottom) projectile

Figure 3 shows the results from the ballistic study. Ballistic limits were taken as the average between the highest impact velocity not giving perforation and the lowest impact velocity giving complete perforation of the target, resulting in $v_{\mathrm{bl}} = 168.0$ m/s for the blunt-nosed and $v_{\mathrm{bl}} = 318.1$ m/s for the ogive-nosed projectile. Note that the ballistic limit for the ogive-nosed projectile is almost twice as high as for the blunt-nosed projectile. The solid lines in Figure 3 are fits to the analytical model of Recht and Ipson [22]

$$v_{\mathrm{r}} = a\left(v_{\mathrm{i}}^{p} - v_{\mathrm{bl}}^{p}\right)^{1/p}, \quad a = \frac{m_{\mathrm{p}}}{m_{\mathrm{p}} + m_{\mathrm{pl}}}, \tag{1}$$

where v_{r} is the residual velocity, v_{i} is the impact velocity, a and p are model constants, m_{p} is the mass of the projectile and m_{pl} is the mass of the plug. For the blunt-nosed projectile in Figure 3, $m_{\mathrm{pl}} \neq 0$ so both $a = 0.70$ and $p = 2.55$ were determined by the fitting procedure, while for the ogive-nosed projectile $m_{\mathrm{pl}} = 0$ so $a = 1$, meaning that only $p = 2.02$ had to be determined by the fitting.

From Figure 3 we see that the residual versus initial velocity curves look dissimilar. The ballistic limit velocity of the 12 mm target plate is much lower when struck by blunt-nosed than by ogive-nosed projectiles. The reason for this is that plugging due to intense plastic localization is the main perforation mechanism in the plates struck by the blunt-nosed projectiles (Figure 4-top). Conversely, radial hole growth is the dominating perforation mechanism of the ogive-nosed projectiles (Figure 4-bottom). The latter requires significant plastic deformation of the high strength steel which dissipates considerable amounts of energy.

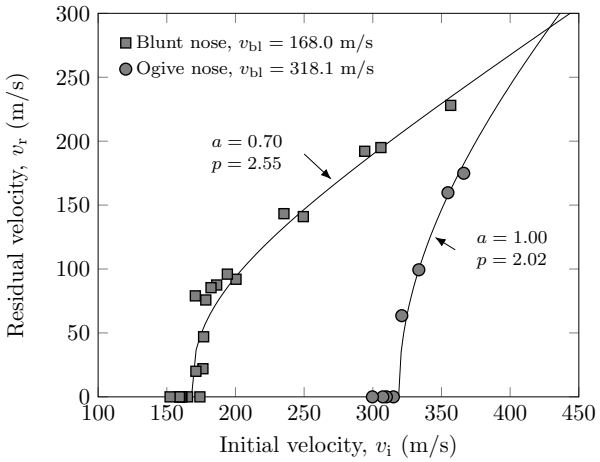

Figure 3: Residual versus initial velocity curves for the different projectiles striking 12 mm thick Weldox 700 E steel plates

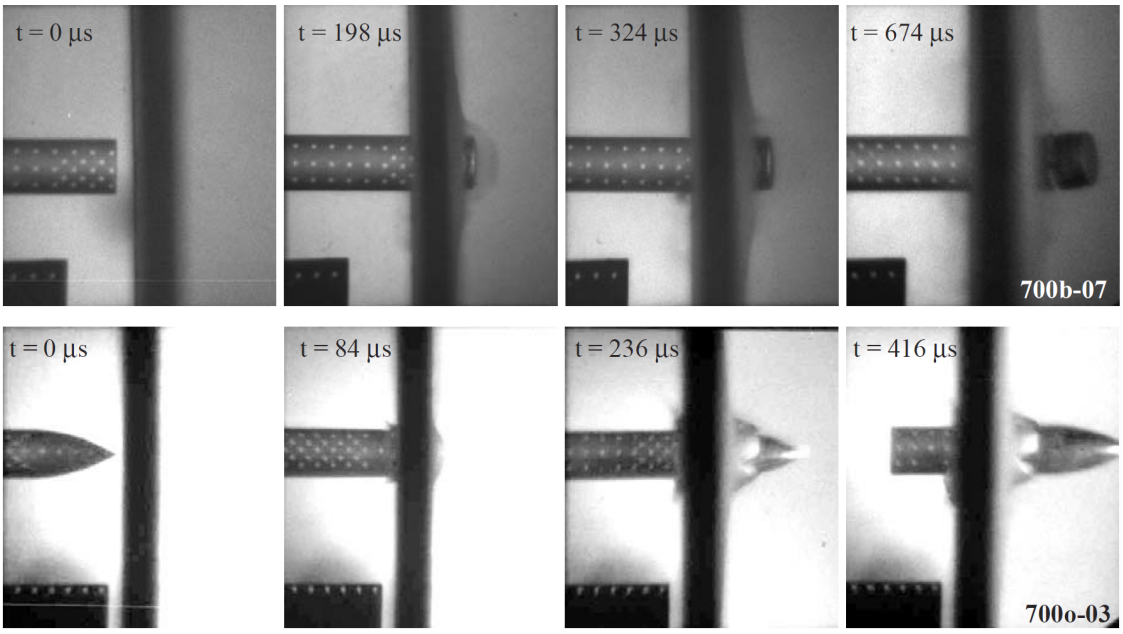

Figure 4: Images captured by the high-speed camera showing perforation of the target plate for the blunt-nosed (top) and ogive-nosed (bottom) projectiles close to their respective ballistic limits [21]

3. Modeling

3.1. Yield surface

The theory of viscoplasticity has three main ingredients: the yield criterion, the flow rule and the constitutive relation. In ballistic impact simulations we also need a failure criterion and an equation of state (here assumed to be linear). This study is primarily concerned with the yield criterion.

The yield criterion, or yield surface, describes the limit at which irreversible or plastic deformations start to appear. Up until this limit the deformations are reversible or elastic. It is formulated as

$$f(\boldsymbol{\sigma}, p, T) = \sigma_{\mathrm{eq}}(\boldsymbol{\sigma}) - \sigma_{\mathrm{y}}(p, T) = 0, \tag{2}$$

where $\boldsymbol{\sigma}$ is the stress tensor, p is the equivalent plastic strain, T is the temperature, and σ_{y} is the quasi-static flow stress. A generalized high-exponent yield function, also known as the Hershey yield function, was used in this study [2, 3]. It is isotropic and pressure independent, and the Hershey equivalent stress is defined in the principal stress space as

$$\sigma_{\mathrm{eq}}(\sigma_1, \sigma_2, \sigma_3) = \left(\frac{1}{2} \left(|\sigma_1 - \sigma_2|^a + |\sigma_2 - \sigma_3|^a + |\sigma_3 - \sigma_1|^a \right) \right)^{\frac{1}{a}}, \tag{3}$$

where σ_1, σ_2, and σ_3 are the principal stresses and $a \geq 1$ determines the curvature of the yield surface. By setting $a = 2$ or $a = 4$ we obtain the von Mises criterion while the yield surface approaches the Tresca criterion by increasing a toward infinity. Figure 5 gives a graphical representation of the shape of the Hershey yield surface in the deviatoric plane for varying values of the parameter a. Note that values of a that are too high might give numerical problems, and also that $a = 1$ gives the original Tresca criterion.

3.2. Thermo-viscoplastic constitutive relation

Usually, materials work harden under plastic deformation, meaning that the yield surface does not only depend on the stress, but also on the accumulated plastic strain. In this study we assume an isotropic evolution of the yield surface in stress space under plastic deformation allowing for an increase of the size of the elastic region while retaining the shape of the yield surface. In addition, the size of the yield surface depends on the temperature, i.e., the elastic domain shrinks with increasing temperature.

A slightly modified version [8] of the well-known model of Johnson and Cook (JC) [6] was used in this work. It is a thermo-viscoplastic constitutive relation that accounts for work hardening, strain-rate hardening and thermal softening. The equivalent plastic strain rate is defined by

$$\dot{p} = \begin{cases} 0 & \text{for } f \leq 0 \\ \dot{p}_0 \left(\left(\dfrac{\sigma_{\mathrm{eq}}(\boldsymbol{\sigma})}{\sigma_{\mathrm{y}}(p, T)} \right)^{1/c} - 1 \right) & \text{for } f > 0 \end{cases} \tag{4}$$

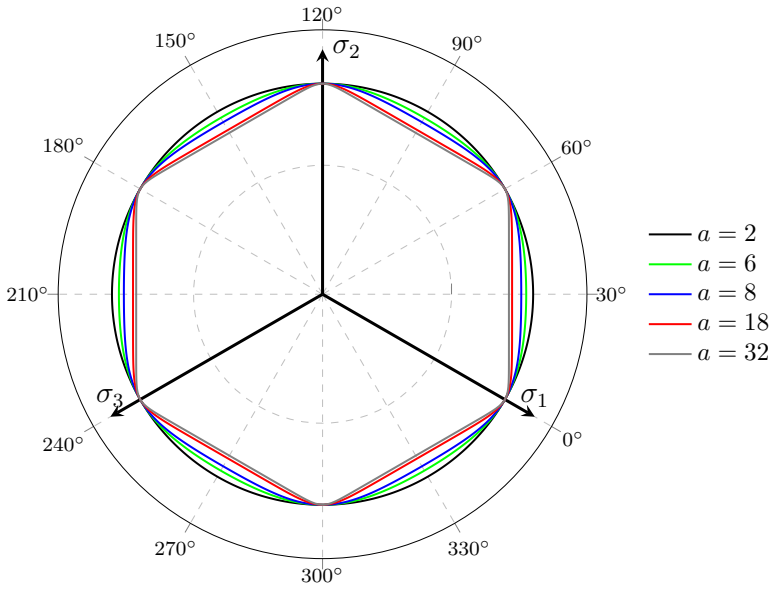

Figure 5: Graphical representation of the shape of the yield surface in the Π-plane. Here, $a = 2$ (outermost locus), 6, 8, 18, and 32 (innermost locus). Note that $a = 2$ corresponds to the von Mises criterion and $a = 32$ resembles the Tresca criterion.

where $\dot{p}_0$ is a reference strain rate and c controls the strain-rate dependence of the material. The quasi-static flow stress is represented by an extended Voce hardening rule which reads

$$\sigma_{\mathrm{y}}(p,T) = \left(A + \sum_{i=1}^{2} Q_i \left(1 - \exp(-C_i p)\right)\right)\left(1 - \left(\frac{T - T_{\mathrm{r}}}{T_{\mathrm{m}} - T_{\mathrm{r}}}\right)^m\right), \tag{5}$$

where A is the initial yield stress, Q_1, C_1, Q_2 and C_2 are parameters controlling the work hardening, T is the current temperature, T_{r} is the ambient temperature, and T_{m} is the melting temperature. The temperature softening is governed by the exponent m. Solving Eq. (4) for the equivalent stress, we get the constitutive relation valid in the viscoplastic regime

$$\sigma_{\mathrm{eq}}(\boldsymbol{\sigma}) = \sigma_{\mathrm{y}}(p,T)\left(1 + \frac{\dot{p}}{\dot{p}_0}\right)^c \quad \text{for } f > 0. \tag{6}$$

In Eq. (6), the first term represents the quasi-static flow stress, including thermal softening, and the second term the strain-rate hardening. In Refs. [21, 23] the quasi-static flow stress of Weldox 700 E was given as a power-rule hardening function. Here, we have converted this to an extended Voce hardening rule by using

a least-squared-fit to the power rule for equivalent plastic strains between 0 and 2. This is not expected to affect the results since the two flow-stress curves are practically indistinguishable. Note also that we in this study use an associated flow rule and that the equivalent stress now is the Hershey equivalent stress and not the von Mises equivalent stress which, as mentioned, is most commonly used in studies of ballistic impact.

The temperature increase due to adiabatic heating was calculated using

$$T = T_{\mathrm{r}} + \int_0^p \frac{\chi}{\rho C_{\mathrm{p}}} \sigma_{\mathrm{eq}} \mathrm{d}p, \tag{7}$$

where ρ is the density, C_{p} is the specific heat, and χ is the Taylor-Quinney coefficient representing the proportion of plastic work that is converted into heat. Assuming adiabatic conditions, the latter is usually set to 0.9.

3.3. Failure criterion

Initiation of failure was determined by the one-parameter criterion of Cockcroft and Latham (CL) [24]. In this criterion, the damage is uncoupled from the constitutive behavior and it accounts for tensile stress and equivalent plastic strain in a cumulative manner:

$$D = \frac{1}{W_{\mathrm{cr}}} \int_0^p \langle \sigma_1 \rangle \, \mathrm{d}p, \qquad \langle \sigma_1 \rangle = \max(\sigma_1, 0), \tag{8}$$

where D is the damage indicator, W_{cr} is the CL failure parameter, and σ_1 is the major principal stress. Damage grows only in the presence of tensile stresses. In numerical simulations, failure is defined as the moment when D becomes 1 in an integration point. The biggest advantages of using the CL failure criterion compared to other criteria are that W_{cr} can be found from a single uniaxial tension test, and that it accounts for the stress triaxiality ratio $\sigma^* = \sigma_{\mathrm{m}}/\sigma_{\mathrm{eq}}$, where σ_{m} is the mean stress, and the Lode parameter $L = (2\sigma_2 - \sigma_1 - \sigma_3)/(\sigma_1 - \sigma_3)$, where $\sigma_1 \geq \sigma_2 \geq \sigma_3$ are the ordered principal stresses. This can be explicitly shown by writing σ_1 as a function of σ^* and L:

$$\sigma_1 = \left(\sigma^* + \frac{3 - L}{3\sqrt{3 + L^2}} \right) \sigma_{\mathrm{eq}}. \tag{9}$$

It transpires that the CL criterion is driven by the plastic work, amplified by a stress state dependent term.

Figure 6 shows the plastic failure strain predicted by the CL criterion as a function of σ^* and L. The shape of the failure surface is similar to the ubiquitous failure model of Johnson and Cook [25], but in addition, the CL criterion accounts for the Lode parameter. According to the CL criterion the failure strain will increase due to temperature softening for elevated temperatures, while the failure strain will decrease due to strain rate hardening for elevated strain rates [26]. Dey et al. [23] found that the CL and JC failure criteria give equally accurate results in simulations of projectile impact of Weldox steel plates.

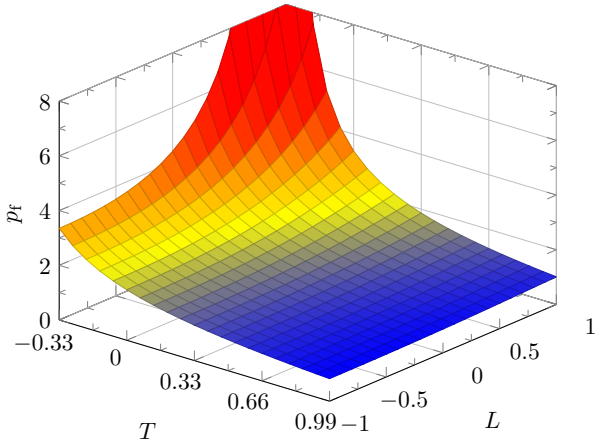

Figure 6: Relationship between the predicted plastic failure strain p_f, stress triaxiality ratio T, and Lode parameter L for the CL failure criterion (W_{cr} = 1424 MPa)

4. Simulations

4.1. Finite element modeling

The explicit solver of the nonlinear finite element code Abaqus/CAE (version 6.14-4) was used to study the effect of the yield surface in the ballistic impact simulations. Since the high-exponent yield criterion, extended Voce hardening rule, and CL failure criterion are not available in Abaqus/CAE, they were implemented in a user-defined subroutine (VUMAT). We used a semi-implicit return-map algorithm with a sub-stepping scheme to ensure stability and accuracy of the computations. Failure was introduced into the numerical model by element erosion, meaning that the stress tensor in an integration point was set to zero when either the CL failure criterion in Eq. (8) was fulfilled, or the temperature exceeded 90 % of the melting temperature of the material.

All the models were three-dimensional and employed mainly 8-node trilinear solid elements with reduced integration (C3D8R). Two symmetry planes were applied in the simulations to save computational

Table 1: Material constants for Weldox 700 E steel [21, 23]

Elastic constants and density			Yield stress and work hardening					Strain rate sensitivity		Temperature softening and adiabatic heating					Failure criterion
E	ν	ρ	A	Q_1	C_1	Q_2	C_2	$\dot{p}_0$	c	T_r	T_m	m	C_p	χ	W_{cr}
(GPa)		(kg/m^3)	(MPa)	(MPa)		(MPa)		(s^{-1})		(K)	(K)		(J/(kg K))		(MPa)
210	0.33	7850	910	598	0.636	203	0.001	5×10^{-4}	0.0115	293	1800	1.071	452	0.9	1424

time. We chose three impact velocities for each nose-shape: 225 m/s, 250 m/s and 350 m/s for the blunt-nosed projectile; and 300 m/s, 350 m/s and 450 m/s for the ogive-nosed projectile. This ensured that we simulated tests both close to, and far above, the ballistic limit velocities of both nose shapes.

All the plate-material parameters required to use the models presented in Section 3 are given in Table 1. They were identified in the literature based on the material tests presented in Section 2.1 [21, 23]. We simplified the behavior of the projectiles to rigid bodies, meaning that we could use the *analytical rigid* option in Abaqus/CAE which speeds up and simplifies the contact calculations. Friction between the projectile and the target has been disregarded in all the simulations, except in Section 5.2, since we seek to compare numerical results to each other, not necessarily compare numerical results to experimental data.

An initial mesh-sensitivity study was conducted to decide the grid size in the main part of the study (Figure 7). The coarsest discretization had 15 elements over the thickness (e.o.t.) corresponding to elements with dimensions 0.8 mm $\times$ 0.8 mm $\times$ 0.8 mm in the impact area. The finest discretization had 120 e.o.t., giving elements with 0.1 mm $\times$ 0.1 mm $\times$ 0.1 mm sides. We used striking velocities of 250 m/s and 350 m/s for the blunt-nosed impactor and 350 m/s and 450 m/s for the ogive-nosed impactor in the mesh-sensitivity study. Yield surface exponents a of 2 and 32 were employed in these simulations.

Figure 7a shows that the residual velocity is strongly affected by the discretization in the case of blunt-nosed projectile impact. The residual velocity increases with increasing refinement, and the effect is strongest for the lowest impact velocity (closer to the ballistic limit velocity). Simulations with the ogive-nosed projectile, shown in Figure 7b, are practically insensitive to the meshes investigated here. Seemingly, it does not matter if we have 15 e.o.t. or 90 e.o.t. for this nose shape. On the other hand, more than 120 e.o.t. are needed to obtain convergence with the blunt-nosed impactor, but 60 e.o.t. will be used in the main study to preserve reasonable computational times. For the ogive-nosed projectile we will use 30 e.o.t. to capture the perforation process. The reason for increased mesh sensitivity in blunt-nosed projectile impact is the strong localization of deformation during the perforation process, while plasticity, which is dominating for

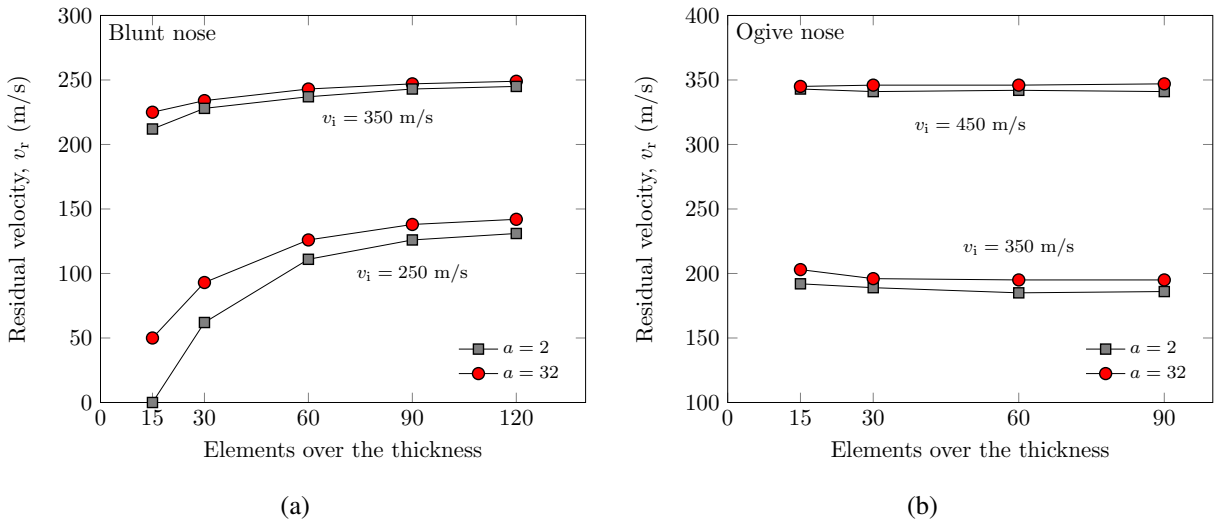

Figure 7: Results from the mesh-sensitivity study with the different impactors and $a = 2$ and $a = 32$

ogive-nosed projectiles, can better be predicted by larger elements. The trends were the same with $a = 2$ and $a = 32$, but the difference between the predicted residual velocities decreased with the element size, especially with the blunt-nosed projectile. This is a result of the increased resistance of the large elements, resulting in lower average velocities during perforation. All effects are larger at low velocities than at high velocities. Simulations by Kane et al. [27] indicated that the mesh sensitivity is not pathological for viscoplastic models, however, to obtain a converged solution the elements must be significantly smaller than what is realistic with the three-dimensional model used in this study.

The computational models are shown in Figure 8 and Figure 9. As already stated, there are 60 and 30 e.o.t. in the models with blunt-nosed and ogive-nosed projectiles, respectively. The refined area has a radius of 15 mm in both cases, the next 10 mm is a transition mesh where the elements gradually get larger until 4 e.o.t. are used in the global part of the plate. The total radius of the plate is 250 mm, and all translational degrees of freedom of the nodes on the circumferential edge are restricted. Note that the peripheral parts of the plate are not expected to contribute much in the energy dissipation due to the highly localized nature of sub-ordnance velocity impact.

4.2. Simulations results

Simulations were run with yield-surface exponents $a = 2$, 6, 8, 18, and 32, as shown in Figure 5. The shape goes from a cylinder, i.e., von Mises, for $a = 2$ toward a Tresca hexagon for $a = 32$. The corners of the yield surface get progressively sharper as a increases. According to Logan and Hosford [28], $a = 8$

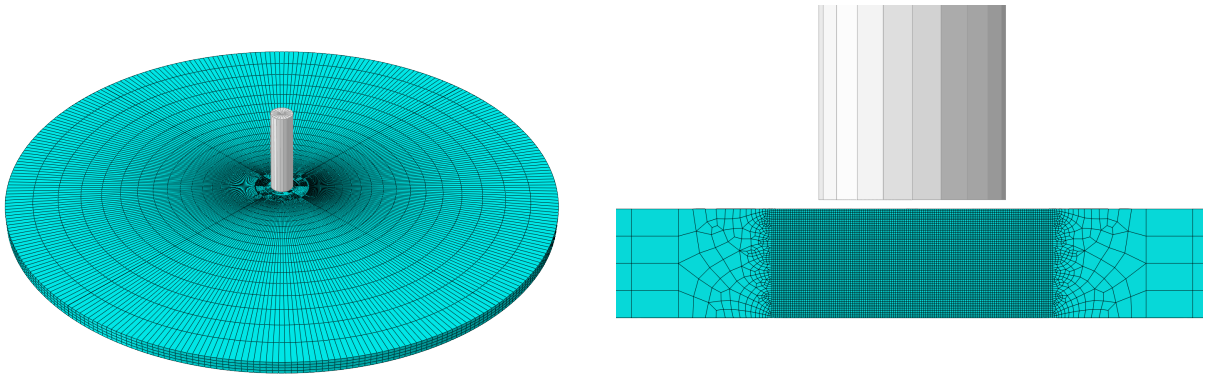

(a) (b)

Figure 8: Images of the finite element model with 60 elements over the thickness and a blunt-nosed projectile. (a) Overview where the model has been mirrored about the two symmetry axes. (b) Close-up of the impact region mirrored about one symmetry axis.

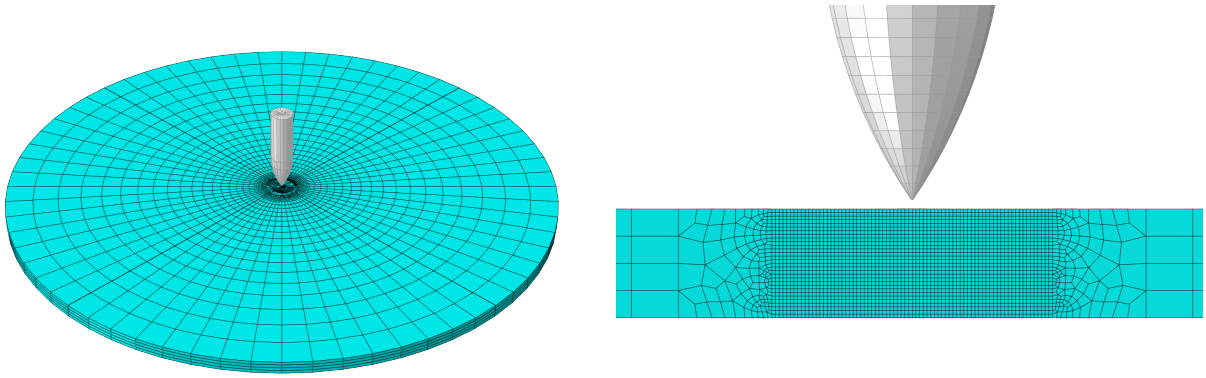

(a) (b)

Figure 9: Images of the finite element model with 30 elements over the thickness and an ogive-nosed projectile. (a) Overview where the model has been mirrored about the two symmetry axes. (b) Close-up of the impact region mirrored about one symmetry axis.

corresponds to face centered cubic materials, such as aluminum, while $a = 6$ corresponds to body centered cubic materials like ferritic steels. The reason why we did not report simulations with $a > 32$ is because the simulations tended to terminate due to numerical errors.

Figure 10a shows how the residual velocity changes as a function of the yield-surface exponent a for the blunt-nosed projectile. The residual velocity increases with the yield-surface exponent, and this trend is more distinct when the initial velocity is low, i.e., close to the ballistic limit velocity. Figure 10b shows how the residual velocity changes as a function of the yield-surface exponent a for the ogive-nosed projectile. Also here, the residual velocity increases with the yield-surface exponent, but not as much as for the blunt-

nosed projectile even though the lowest initial velocity is extremely close to the ballistic limit velocity.

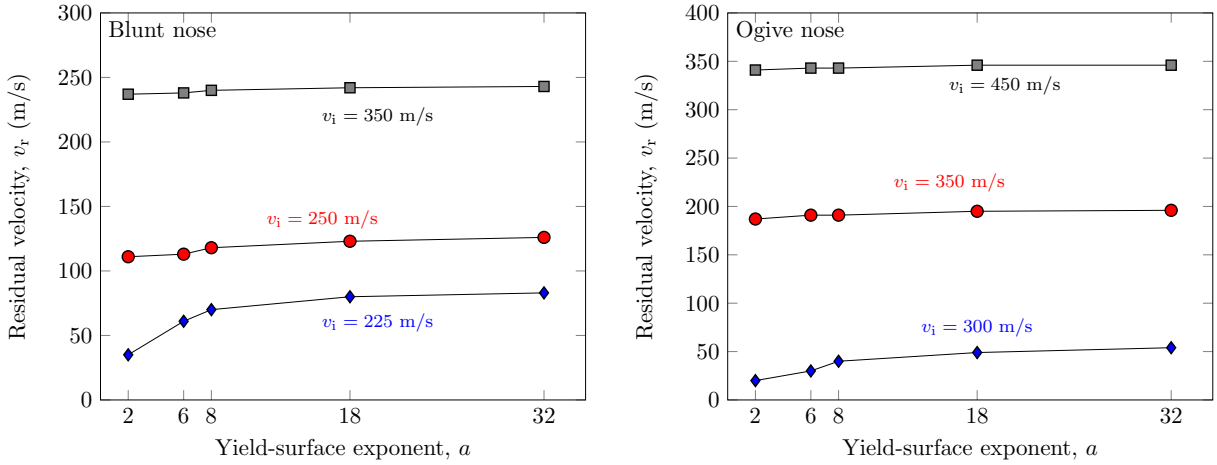

(a) (b)

Figure 10: The effect of the yield-surface exponent a on the residual velocity of (a) a blunt-nosed projectile and (b) an ogive-nosed projectile striking a 12 mm thick Weldox 700 E steel plate

The contrasting perforation mechanisms that are induced by the different nose shapes are readily identified in the simulation sequences in Figure 11 and Figure 12. For the blunt-nosed projectile the plastic strain is restricted to a small area close to the projectile and a plug is punched out from the plate. For the ogive-nosed projectile the plastic strain is more spread out and it is clear that the plastic deformation covers a larger area for this nose shape. Simulations using the blunt-nosed projectiles (Figure 11) and simulations using the ogive-nosed projectile (Figure 12) both capture the main perforation mechanisms seen for the corresponding nose shapes in Figure 4.

The goal of conducting ballistic simulations is often to determine the ballistic limit velocity or, in other words, the capacity of the target. If we use the Recht-Ipson relation in Eq. (1) based on the three data points we have for each configuration from the simulations, we can estimate the ballistic capacity. Figure 13 shows the simulation results plotted as residual versus initial velocity curves. The estimated ballistic limit velocities vary more with the yield surface exponent for the blunt-nosed projectile than for the ogive-nosed projectile. Specifically, $v_{bl} = 223.2$ m/s for $a = 2$, while $v_{bl} = 208.5$ m/s for $a = 32$ giving a variation of 6.6 % in case of the blunt nose. For the ogive nose, $v_{bl} = 300.0$ m/s for $a = 2$, whereas $v_{bl} = 296.0$ m/s for $a = 32$, a difference of only 1.3 %, which, in practice, is negligible. The predicted capacity decreases as the yield-surface exponent increases, i.e., when the corners of the yield surface becomes sharper.

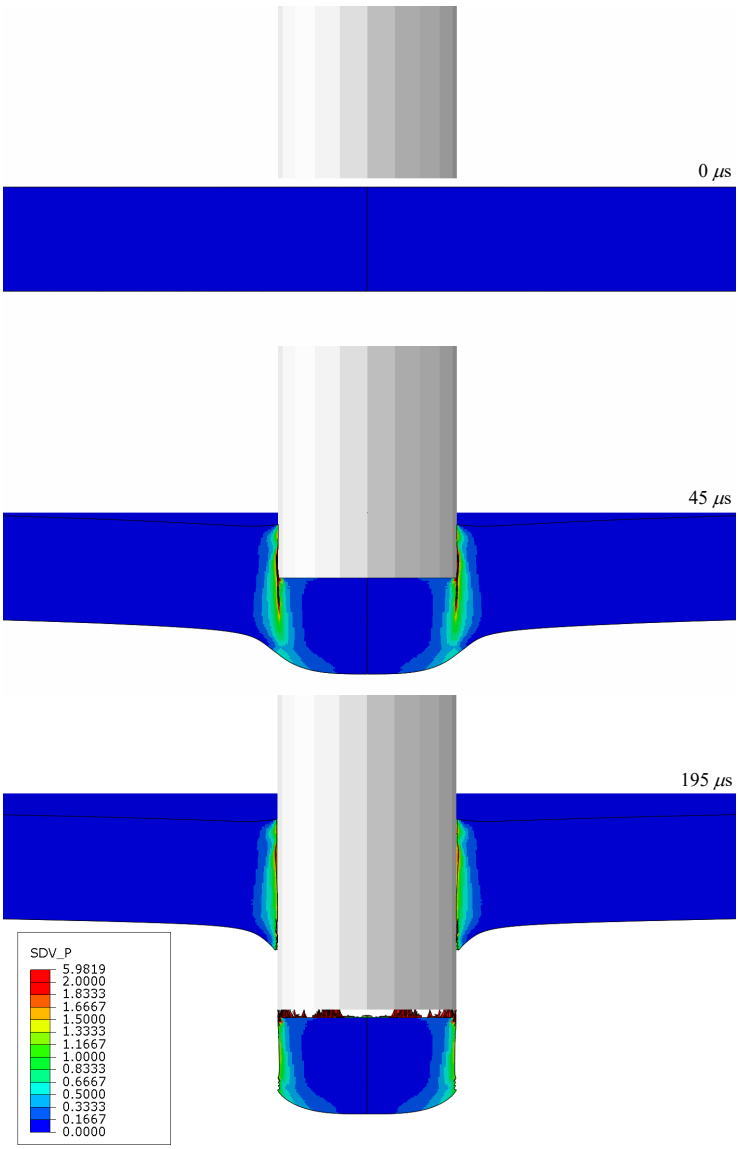

Figure 11: Simulation sequence shown for a blunt-nosed projectile with 60 elements over the thickness, $a = 2$, $v_\mathrm{i} = 250$ m/s, $v_\mathrm{r} = 111$ m/s. The fringes show accumulated plastic strain and the model is mirrored about a symmetry axis.

5. Discussion

5.1. Comparison to the experiments

The experimental work recapitulated in Section 2.2 identified ballistic limit velocities of 168.0 m/s for the blunt-nosed projectile and 318.1 m/s for the ogive-nosed impactor. In the numerical simulations presented in Section 4.2 we overestimated the ballistic limit velocity for the blunt-nosed projectile by 32.9

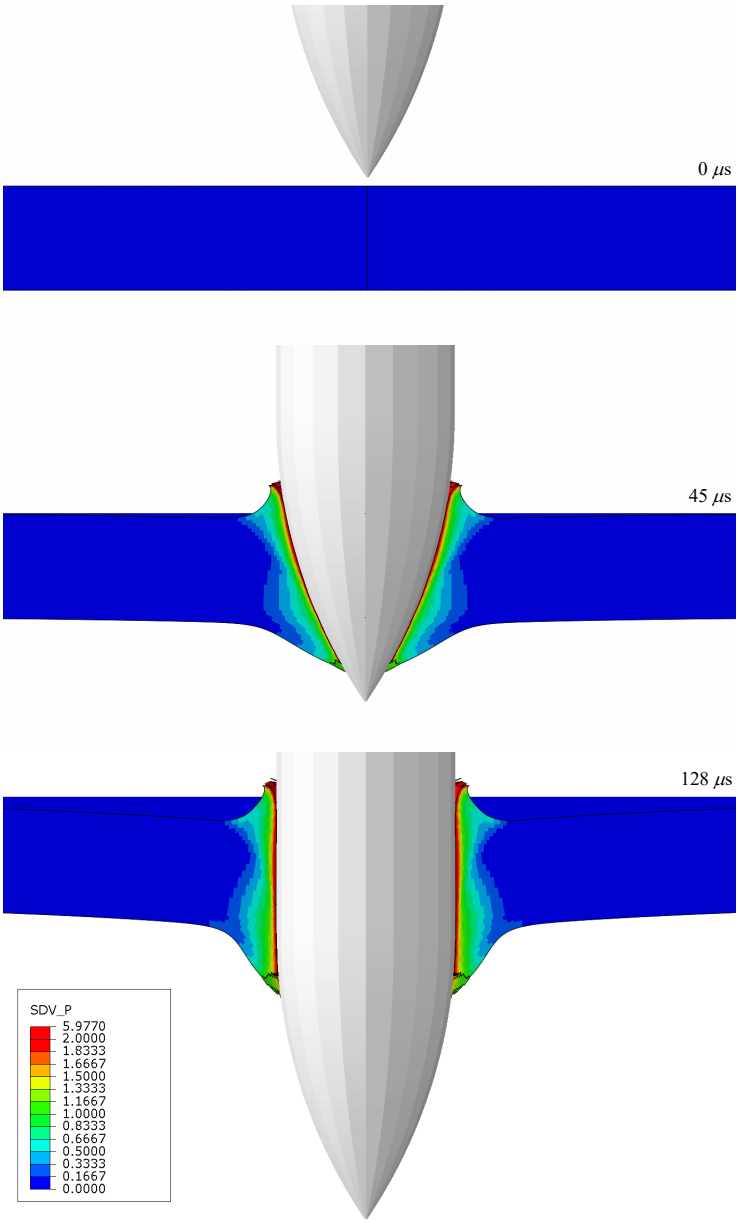

Figure 12: Simulation sequence shown for a ogive-nosed projectile with 30 elements over the thickness, $a = 2$, $v_i = 350$ m/s, $v_r = 189$ m/s. The fringes show accumulated plastic strain and the model is mirrored about a symmetry axis.

% with $a = 2$ ($v_{bl} = 223.2$ m/s). The overestimation is smaller with higher yield-surface exponents, and it reduces to 24.1 % for $a = 32$ ($v_{bl} = 208.5$ m/s). This is similar to the 2D axisymmetric simulations of Weldox 700 E (using LS-DYNA) presented by Dey et al. [21] where they predicted a ballistic limit velocity of $v_{bl} = 211.7$ m/s. The reason for the discrepancy between simulations and experiments is probably that the dominating perforation mechanism is localized shear with a shear band much narrower than the minimum

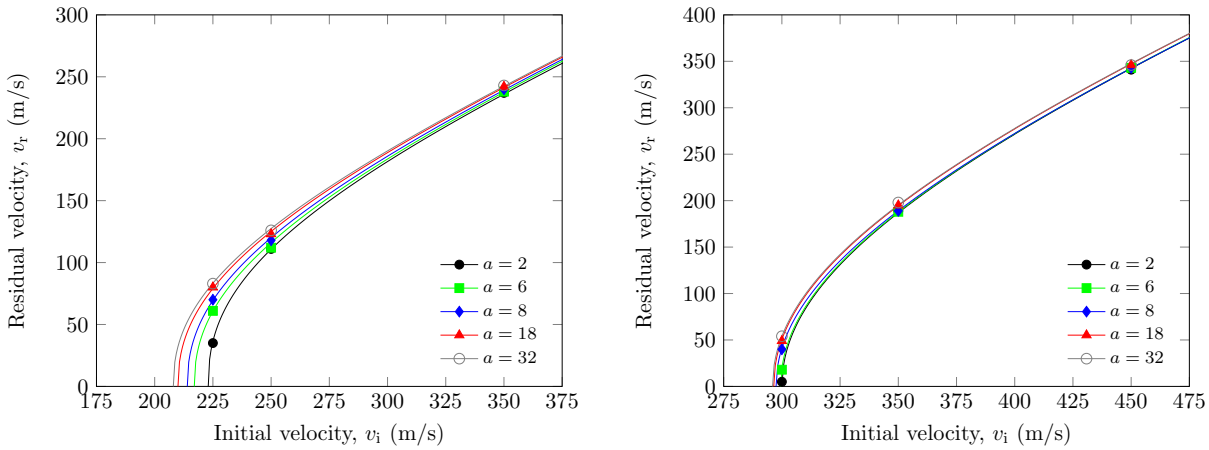

Figure 13: Estimated residual velocity versus initial velocity curves for (a) blunt-nosed projectiles and (b) ogive-nosed projectiles based on the simulations with various yield-surface exponents

element size; thus, the localization has not been fully captured in the simulations. The localized shear bands in Weldox 700 E steel plates struck by blunt-nosed projectiles have been found to be thinner than 10 μm [21]. Since we in this study employed 3D brick elements, a sufficiently fine mesh is unrealistic. Even in Dey et al. [21] and Kane et al. [27] where they used 2D axisymmetric elements, a sufficiently fine mesh was not obtained.

The results from the simulations with the ogive-nosed projectiles were closer to their experimental counterparts than the simulations with the blunt-nosed projectile. With $a = 2$ the ballistic limit velocity was $v_{\text{bl}} = 300.0$ m/s while the ballistic limit velocity barely decreased to $v_{\text{bl}} = 296.0$ m/s for $a = 32$. The relative errors from the experiments for these configurations are -5.7 % and -6.9 %, respectively, i.e., small underestimations of the capacity of the plate. Dey et al. [21] did not present results from simulations on ogive-nosed projectiles, but their results from impacts by conical-nosed projectiles were of similar accuracy as our results with an ogive-nosed projectile.

The reason why we ran 3D simulations and not 2D axisymmetric simulations in this study is that we encountered numerical problems in the simulations of impacts with ogive-nosed projectiles with 2D axisymmetry. Remedying this requires re-meshing during the simulation which greatly complicates the simulations process. Also, 3D simulations are the rule and not the exception in these types of problems.

5.2. *Implications of other parameters*

To put the effects of changing the shape of the yield surface into a broader context, we assessed its implications in light of other parameters in the finite element models. The strain-rate sensitivity exponent c, temperature softening exponent m, Taylor-Quinney coefficient χ, and the friction coefficient μ were varied in a series of simulations. The reason for investigating these parameters in particular, is that they are often subjected to uncertainties in the modeling of ballistic impact and often just taken from literature. An impact velocity of 250 m/s was chosen for the blunt-nosed projectile and 350 m/s was chosen for the ogive-nosed projectile.

Figure 14 shows, for various a, residual velocities normalized with respect to the residual velocities from the simulations with $a = 2$. The residual velocities increase by a maximum of 11.4 % and 4.8 % for the blunt-nosed and ogive-nosed projectiles, respectively. Note that normalized residual velocities higher than 1.0 indicate less resistance in the model (lower capacity), and that normalized residual velocities lower than 1.0 indicate more resistance in the model (higher capacity).

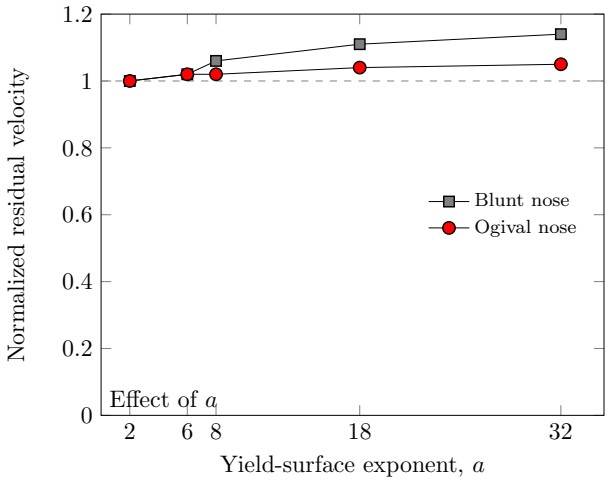

Figure 14: Effect of the yield-surface exponent on the normalized residual velocity; v_i = 250 m/s for the blunt-nosed projectile and v_i = 350 m/s for the ogive-nosed projectile

In Figure 15, we present the results from simulations where the selected parameters were varied. As seen in Figure 15a, the strain-rate sensitivity exponent c is important for the residual velocity. Assigning values of c between 0.001 and 0.02 gives residual velocities ±17 % from the baseline simulation. If we increase it further, to the rather unphysical value of 0.05, the plate stops the projectile. The strain-rate sensitivity exponent has a similar effect on the results for both the blunt-nosed and ogive-nosed projectile.

Note that the strain-rate sensitivity exponent c in the constitutive equation in Eq. (4) is not identical to the strain-rate sensitivity coefficient in the original JC model, but these results should also apply for the original JC model since their effects are similar.

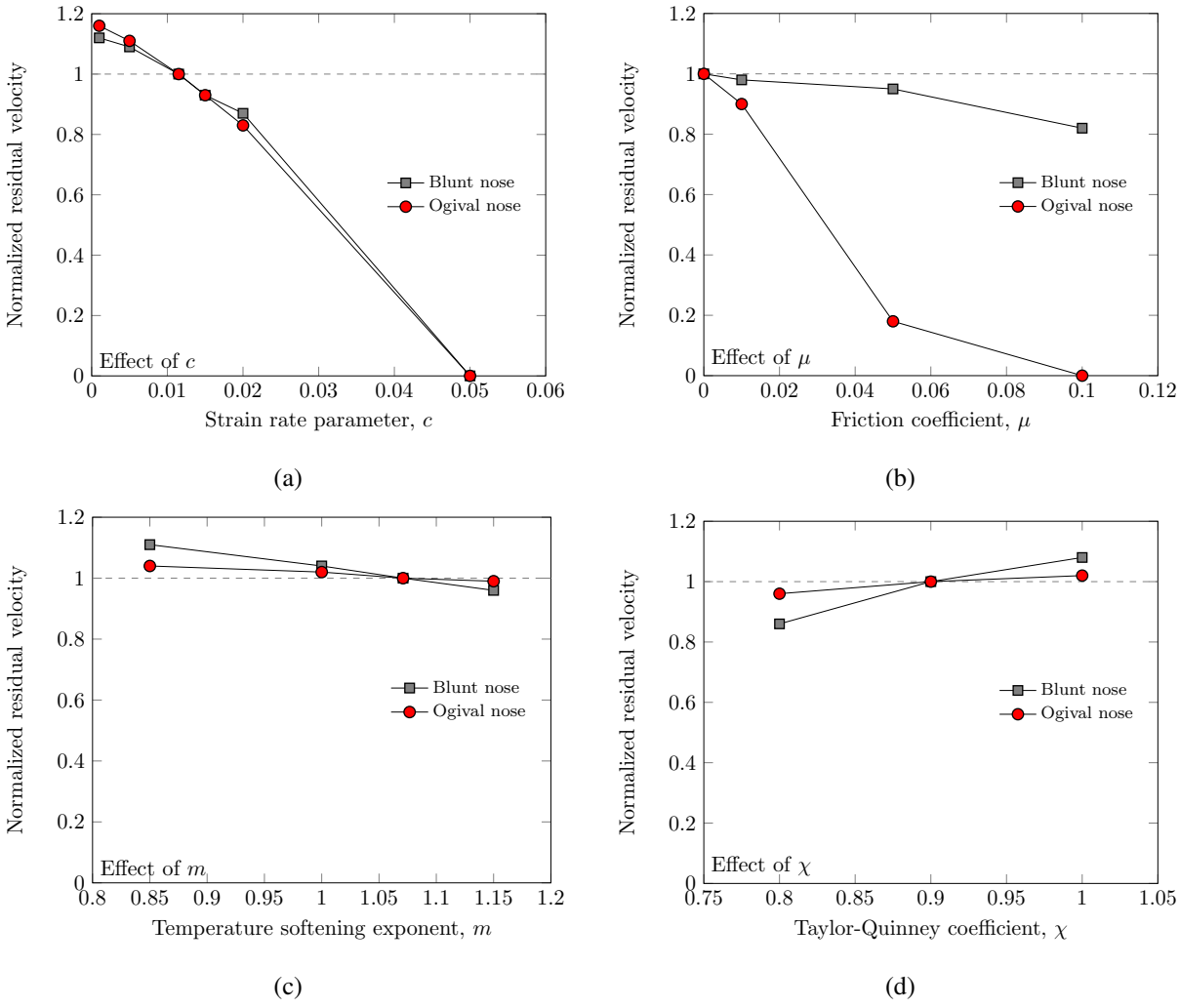

Figure 15: Effects of the selected parameters in impact simulations. v_i = 250 m/s for the blunt-nosed projectile and v_i = 350 m/s for the ogive-nosed projectile using a yield-surface exponent $a = 2$ in all cases. (a) Effect of strain-rate exponent, (b) effect of friction coefficient, (c) effect of temperature softening exponent, and (d) effect of the Taylor-Quinney coefficient.

The friction coefficient μ increases the resistance to perforation slightly for the blunt-nosed projectile (Figure 15b). When $\mu = 0.1$, which is probably unrealistically high in a perforation problem [29], the residual velocity is 18 % lower than with no friction at all. However, the results with the ogive nose are extremely dependent upon μ since the projectile is always in contact with the plate due to the ductile hole

growth perforation mechanism. At $\mu = 0.05$ the residual velocity is 82 % lower than the residual velocity with no friction at all, and at $\mu = 0.1$ the projectile is completely stopped by the plate. Thus, μ has a much stronger effect on simulations with ogive-nosed projectiles than on simulations with blunt-nosed projectiles. Note that we have used Coulomb friction without a cut-off value, meaning that the frictional forces are not limited from above.

Figure 15c illustrates that the temperature softening exponent m hardly influences the results for the ogive-nosed projectile, but that it slightly affects the results with the blunt-nosed projectile. By keeping m between 0.85 and 1.15, which covers most steels and aluminum alloys, the results vary from 11 % higher to 4 % lower than the basis simulation in this paper. The reason why a higher m gives lower residual velocities is that the thermal softening is reduced with increasing values of m.

The residual velocity increases with the Taylor-Quinney coefficient χ (Figure 15d). Also here the effect is largest for the blunt-nosed projectile. The coefficient determines the percentage of plastic work that turns into heat and is usually assumed to be 0.9 in numerical simulations of ballistic impact. We find that $\chi = 0.8$ gives 14 % lower residual velocity while $\chi = 1.0$ gives 8 % higher residual velocity than $\chi = 0.9$ for the blunt nose. Here, high χ gives faster temperature increase in the model. The ogive-nosed projectile results are nearly insensitive to this parameter.

The preceding discussion highlighted that projectile nose shape influences how different input parameters affect the simulation results. If the yield surface is allowed to vary between the von Mises and Tresca yield surfaces, i.e., between the two extremes, the shape of the yield surface can be equally important as the strain-rate sensitivity exponent c, temperature softening exponent m, Taylor-Quinney coefficient χ, and friction coefficient μ if they are kept within the range that can be expected for common steels and aluminum alloys.

6. Concluding remarks

The numerical simulations in this study were conducted to elucidate how the yield-surface shape influences the results of ballistic impact simulations of steel plates. An extensive experimental ballistic study, with both blunt-nosed and ogive-nosed projectiles, from the literature was used to put the simulations into context. Since strong shear localization is difficult to capture numerically, simulations of the projectile with the blunt nose overestimated the capacity of the plates by as much as 30 % while the simulations of the projectile with the ogive nose were within 7 %.

By increasing the yield-surface exponent, i.e., making the corners of the yield surface sharper, we observed an increase in the residual velocity. This consequently led to a lower predicted capacity of the target plate. The effect of the yield surface in terms of ballistic limit velocity was significant for the blunt-nosed projectile (as much as 7 %), but practically insignificant for the ogive-nosed projectile.

The residual velocity is hardly affected by the shape of the yield surface at high impact velocities. However, close to the ballistic limit the residual velocity can vary significantly with yield-surface shape, especially for the blunt-nosed projectile. Although the residual velocity close to the ballistic limit velocity is influenced by the yield surface exponent, our results suggest that to determine the ballistic limit, or to predict residual velocities far from the ballistic limit, a von Mises yield surface gives adequate results. Thus, a high-exponent yield surface is not of major importance in ballistic impact simulations, at least for moderate yield surface exponents that we expect for most aluminum alloys and steels.

Acknowledgment

This financial support for this work comes from Centre for Research-based Innovation scheme through Centre for Advanced Structural Analysis (CASA).

References

[1] Drucker DC, Prager W. Soil mechanics and plastic analysis for limit design. Quarterly of Applied Mathematics 1952;10:157–65.

[2] Hershey AV. The plasticity of an isotropic aggregate of anisotropic face centered cubic crystals. Journal of Applied Mechanics 1954;21:241–9.

[3] Hosford WF. A generalized isotropic yield criterion. Transactions of the ASME Series E Journal of Applied Mechanics 1972;39:607–9.

[4] Hill R. A theory of the yielding and plastic flow of anisotropic metals. Proceedings of the Royal Society of London A 1947;193:281–97.

[5] Barlat F, Aretz H, Yoon JW, Karabin ME, Brem JC, Dick RE. Linear transformation-based anisotropic yield functions. International Journal of Plasticity 2005;21:1009–39.

[6] Johnson GR, Cook WH. A constitutive model and data for metals subjected to large strains, high strain rates and high temperatures. In: Proceedings of the 7th International Symposium on Ballistics. 1983, p. 541–7.

[7] Børvik T, Langseth M, Hopperstad OS, Malo KA. Ballistic penetration of steel plates. International Journal of Impact Engineering 1999;22:855–86.

[8] Børvik T, Hopperstad OS, Berstad T, Langseth M. A computational model of viscoplasticity and ductile damage for impact and penetration. European Journal of Mechanics A/Solids 2001;20:685–712.

[9] Børvik T, Hopperstad OS, Langseth M, Malo KA. Effects of target thickness in blunt projectile penetration of Weldox 460 E steel plates. International Journal of Impact Engineering 2003;28:413–64.

[10] Holmen JK, Johnsen J, Hopperstad OS, Børvik T. Influence of fragmentation on the capacity of aluminum alloy plates subjected to ballistic impact. European Journal of Mechanics A/Solids 2016;55:221–33.

[11] Arias A, Rodriguez-Martinez JA, Rusinek A. Numerical simulations of impact behaviour of thin steel plates subjected to cylindrical, conical and hemispherical non-deformable projectiles. Engineering Fracture Mechanics 2008;75:1635–56.

[12] Iqbal MA, Gupta G, Diwakar A, Gupta N. Effect of projectile nose shape on the ballistic resistance of ductile targets. European Journal of Mechanics A/Solids 2010;29:683–94.

[13] Iqbal MA, Chakrabarti A, Beniwal S, Gupta NK. 3D numerical simulations of sharp nosed projectile impact on ductile targets. International Journal of Impact Engineering 2010;37:185–95.

[14] Manes A, Serpellini F, Pagani M, Saponara M, Giglio M. Perforation of aluminium target plates by armour piercing bullets. International Journal of Impact Engineering 2014;69:39–54.

[15] Aune V, Valsamos G, Casadei F, Larcher M, Langseth M, Børvik T. Numerical study on the structural response of blast-loaded thin aluminium and steel plates. International Journal of Impact Engineering 2017;99:131–44.

[16] Bai Y, Wierzbicki T. A new model of metal plasticity and fracture with pressure and Lode dependence. International Journal of Plasticity 2008;24:1071–96.

[17] Chocron S, Erice B, Anderson CE. A new plasticity and failure model for ballistic application. International Journal of Impact Engineering 2011;38:755–64.

[18] Grytten F, Børvik T, Hopperstad OS, Langseth M. Low velocity perforation of AA5083-H116 aluminium plates. International Journal of Impact Engineering 2009;36:597–610.

[19] Seidt JD, Pereira JM, Gilat A, Revilock DM. Ballistic impact of anisotropic 2024 aluminum sheet and plate. International Journal of Impact Engineering 2013;62:27–34.

[20] Barlat F, Lege DJ, Brem JC. A six-component yield function for anisotropic materials. International Journal of Plasticity 1991;7:693–712.

[21] Dey S, Børvik T, Hopperstad OS, Leinum JR, Langseth M. The effect of target strength on the perforation of steel plates using three different projectile nose shapes. International Journal of Impact Engineering 2004;30:1005–38.

[22] Recht RF, Ipson TW. Ballistic perforation dynamics. Journal of Applied Mechanics 1963;30:384–90.

[23] Dey S, Børvik T, Hopperstad OS, Langseth M. On the influence of fracture criterion in projectile impact of steel plates. Computational Materials Science 2006;38:176–91.

[24] Cockcroft MG, Latham DJ. Ductility and the workability of metals. Journal of the Institute of Metals 1968;96:33–9.

[25] Johnson GR, Cook WH. Fracture characteristics of three metals subjected to various strains, strain rates, temperatures and pressures. Engineering Fracture Mechanics 1985;21:31–48.

[26] Holmen JK, Solberg JK, Hopperstad OS, Børvik T. Ballistic impact of layered and case-hardened steel plates. International Journal of Impact Engineering 2017;N/A:N/A. doi:10.1016/j.ijimpeng.2017.02.001.

[27] Kane A, Børvik T, Hopperstad OS, Langseth M. Finite element analysis of plugging failure in steel plates struck by blunt projectiles. Journal of Applied Mechanics 2009;76:051302 1–11.

[28] Logan RW, Hosford WF. Upper-bound anisotropic yield locus calculations assuming <111>-pencil glide. International Journal of Mechanical Sciences 1980;22:419–30.

[29] Børvik T, Langseth M, Hopperstad OS, Malo KA. Perforation of 12 mm thick steel plates by 20 mm diameter projectiles with flat, hemispherical and conical noses. Part I: Experimental study. International Journal of Impact Engineering 2002;27:19–35.